Supporting Information

A Unified Theory of Electron-Rich and Electron-Deficient Multicenter Bonds in Molecules and Solids: A Change of Paradigms

H. H. Osman[1,2,3]*, P. Rodríguez-Hernández[4], A. Muñoz[4], and F. J. Manjón[1]*

[1] Instituto de Diseño para la Fabricación y Producción Automatizada, MALTA Consolider Team, Universitat Politècnica de València, 46022, València, Spain.

[2] Instituto de Ciencia de los Materiales de la Universitat de València, MALTA Consolider Team, Universitat de València, 46100, Burjassot, Valencia, Spain.

[3] Chemistry Department, Faculty of Science, Helwan University, 11795, Cairo, Egypt.

[4] Departamento de Física, MALTA Consolider Team, Universidad de La Laguna, 38205, La Laguna, Tenerife, Spain.

*Corresponding author(s). E-mail(s): hussien.helmy@uv.es and fjmanjon@fis.upv.es

1. Computational details

First-principles calculations for solids were performed using the density-functional theory (DFT) as implemented in the Vienna Ab initio Simulation Package (VASP).[1–3] All calculations were implemented at the generalized gradient approximation (GGA) level, using the Perdew–Burke–Ernzerhof (PBE) exchange-correlation functional[4] with the projector augmented-wave (PAW) method.[5] In most cases, the PBE functional revised for solids (PBEsol)[6] has provided improved structural parameters that reasonably agree with the corresponding experimental results as shown in **Table S1**. Brillouin-zone integrals were approximated using Γ-centered Monkhorst–Pack meshes.[7] The wavefunction was expanded in plane waves up to a certain cutoff energy to ensure convergence of the total energy within 10^{-5} eV per atom. Details of k-point meshes, planewave cutoff energies (E_{cutoff}), and experimental and calculated lattice parameters are given in **Table S1**.

A density-based method based on the Quantum Theory of Atoms in Molecules (QTAIM) has been used to analyze the topology of the electron density in the solids studied in this work. For this purpose, Quantum ESPRESSO, version 6.5,[8] was used in combination with wannier90[9] and the CRITIC2 program.[10] For this purpose, single-point calculations at the VASP equilibrium geometries were carried out using the same uniform k-point grids as in VASP calculations, a plane-wave cutoff of 80 Ry and a density cutoff of 320 Ry were used for all calculations. Both the norm-conserving pseudopotentials (for the Kohn-Sham states) and the PAW[5] data sets (for the all-electron density) were obtained from the pslibrary.[11] Delocalization index (DI) calculations, used to calculate the number of electrons shared (ES) as 2 × DI, were carried out using a Wannier transformation as detailed in Ref. [12]. **Table S2** summarizes the density-based calculated quantum-chemical bonding descriptors for the compounds studied in this work.

On the other hand, an orbital-based method has also been used to analyze the topology of the electron density in the solids studied in this work. For this purpose, the *Local Orbital Basis Suite Towards Electronic-Structure Reconstruction* (LOBSTER) package was used.[13–15] In this case, the number of electrons shared (ES) was calculated as 2 × ICOBI, where ICOBI stands for the integrated Crystal Orbital Bond Index as detailed in Ref. [16]. **Table S3** summarizes the orbital-based calculated quantum-chemical bonding descriptors for the compounds studied in this work.

Additional QTAIM calculations were performed for some molecules, such as the I_3^-, XeF_2, F_2H^- and B_2H_6. Simulations for these molecules were performed at the B3LYP/def2-QZVPP level[17,18] and the DIs were obtained using the density-based AIMAll code.[19]

2. Results
2.1. Tables.

Table S1. Computational details of VASP calculations for the solids studied in this work, cutoff energy (E_{cutoff}) and *k*-mesh including experimental and calculated lattice parameters and unit cell volume.

Species	Space group	E_{cutoff} (ev)	*k*-mesh	lattice parameters (Å) (*a, b, c*)		unit cell volume (Å³)	
				Exp.	Calc.	Exp.	Calc.
CsI_3	*Pnma* (62)	350	4 × 6 × 4	11.086 6.844 10.027[20]	10.897 6.793 10.093	760.88[20]	747.12
Cs_2Te_5	*Cmcm* (63)	400	4 × 4 × 3	9.373 12.288 10.140[21]	9.602 12.092 10.294	1167.88[21]	1195.15
Cs_2TeI_6	*Fm-3m* (225)	350	6 × 6 × 6	11.700[22]	11.602	1601.61[22]	1561.63
TeI_4	*P-1* (2)	250	6 × 4 × 4	7.885 10.702 10.749 (α=85.66° β=71.79° γ=71.56°)[23]	7.794 10.676 10.729 (α=86.86° β=73.39° γ=72.44°)	817.12[23]	815.28
Li_2Sb	*P-62m* (189)	250	6 × 6 × 12	7.947 7.947 3.260[24]	7.864 7.864 3.237	178.30[24]	173.39
$BaZnSb_2$	*I4/mmm* (139)	400	11 × 11 × 16	4.584 4.584 23.050[25]	4.451 4.451 23.423	484.65[25]	464.04
⍺-GeTe	*R3m* (160)	450	14 × 14 × 5	4.174 4.174 10.692[26]	4.169 4.169 10.423	161.29[26]	156.88
SnSe	*Cmcm* (63)	350	3 × 8 × 7	4.274 11.643 4.296[27]	4.012 10.924 4.051	213.78[27]	212.29
TeO_2	*P41 21 2* (92)	560	6 × 6 × 4	4.805 4.805 7.602[28]	4.828 4.282 7.452	175.53[28]	173.68
$SbPO_4$	*P1 21/m1* (11)	550	5 × 4 × 5	5.103 6.772 4.744 (β= 94.61°)[29]	5.041 6.822 4.739 (β= 97.13°)	163.42[29]	161.72
$Sc_2Si_2O_7$	*C1 2/m 1* (12)	500	5 × 4 × 5	6.530 8.521 4.681 (β= 102.63°)[30]	*6.490 8.523 4.710 (β= 102.71°)*	254.15[30]	254.15
HF	*Cmc21* (36)	550	9 × 9 × 7	3.310 5.220 4.260[31]	*3.410 5.572 4.060*	73.605[31]	77.142
TlTe	*I4/mcm* (140)	400	8 × 8 × 5	12.953 12.953 6.173[32]	12.963 12.963 6.102	1035.71[32]	1025.34

Table S2. Calculated quantum-chemical bonding descriptors for selected systems discussed in section 4 of the main text using the density-based approach QTAIM as implemented in CRITIC2 software. The Bader atomic charges for the different Wyckoff sites, the renormalized number of electrons transferred between two atoms (ET), and the number of electrons shared between each atom pair (ES) are provided as well as the bond distances and the bond types. The ES is defined as 2×DI, where DI is the delocalization index between two atoms.

Species	Bader charge (Wyck)		ET		ES (2 × DI)		Bond distance (Å)	Bond type
I_3^- (I_1–I_2–I_3)$^-$	I_1	−0.48	I_1–I_2	0.44	I_1–I_2	1.85	2.875	ERMB
	I_2	−0.04	I_2–I_3	0.44	I_2–I_3	1.53	2.954	ERMB
	I_3	−0.48						
XeF_2	Xe	+1.24	Xe–F	0.62	Xe–F	1.76	1.983	ERMB
	F	−0.62						
FHF^-	F	−0.85	F-H	0.70	F-H	1.68	1.148	ERMB
	H	+0.70						
B_2H_6	B	+1.80	B–H_1	0.63	B–H_1	0.68	2.478	EDMB
	H_1	−0.63	B–H_2	0.59	B–H_2	1.20	2.238	Covalent
	H_2	−0.59						
BH_3	B	+1.84	B–H	0.61	B–H	1.25	1.187	Covalent
	H_1	−0.61						
	H_2	−0.61						
	H_3	−0.61						
CsI_3 (I_1–I_2–I_3)$^-$	Cs (*4c*)	+0.73	I_1–I_2	0.36	I_1–I_2	1.53	2.870	ERMB
	I_1 (*4c*)	−0.39	I_2–I_3	0.28	I_2–I_3	1.85	2.990	ERMB
	I_2 (*4c*)	−0.03	Cs–I	0.73	Cs–I	0.14	3.755	Ionic
	I_3 (*4c*)	−0.31						
Cs_2Te_5	Cs_1 (*4c*)	+0.71	Te_1–Te_2	0.39	Te_1–Te_2	1.43	3.060	ERMB
	Cs_2 (*4c*)	+0.69	Te_2–Te_2	0.00	Te_2–Te_2	2.20	2.820	Covalent
	Te_1 (*4c*)	+0.03						
	Te_2 (*16h*)	−0.36						
Cs_2TeI_6	Cs (*8c*)	+0.76	Te–I	0.52	Te–I	1.42	2.925	ERMB
	Te (*4a*)	+0.82	Cs–I	0.76	Cs–I	0.08	4.099	Ionic
	I (*24e*)	−0.39						
TeI_4	Te_1 (*2i*)	+0.75	Te_1–I_1	0.12	Te_1–I_1	1.88	2.799	Covalent
	Te_2 (*2i*)	+0.76	Te_1–I_2	0.18	Te_1–I_2	1.95	2.772	Covalent
	I_1 (*2i*)	−0.12	Te_2–I_8	0.16	Te_2–I_8	1.98	2.760	Covalent
	I_2 (*2i*)	−0.18						
	I_3 (*2i*)	−0.21						
	I_4 (*2i*)	−0.23						
	I_5 (*2i*)	−0.26						
	I_6 (*2i*)	−0.18						
	I_7 (*2i*)	−0.17						
	I_8 (*2i*)	−0.16						
Li_2Sb	Li_1 (*3f*)	+0.81	Sb_1–Sb_1	0.0	Sb_1–Sb_1	1.40	3.160	EDMB
	Li_2 (*3g*)	+0.83	Sb_2–Sb_2	0.0	Sb_2–Sb_2	1.40	3.160	EDMB
	Sb_1 (*1b*)	−1.67						
	Sb_2 (*2c*)	−1.63						
$BaZnSb_2$	Ba (*4e*)	+1.36	Sb_1–Sb_1	0.0	Sb_1–Sb_1	1.16	3.242	EDMB
	Zn (*4d*)	+0.15	Zn–Sb_2	0.53	Zn–Sb_2	1.14	2.770	Covalent
	Sb_1 (*4c*)	−0.60	Ba–Sb	0.68	Ba–Sb	0.22	3.486	Ionic
	Sb_2 (*4e*)	−0.91						
⍰-GeTe	Ge (*3a*)	+0.36	Ge–Te	0.18	Ge–Te	1.16	2.848	EDMB
	Te (*3a*)	−0.36						
SnSe	Sn (*4c*)	+0.80	Sn–Se	0.4	Sn–Se (ax)	1.10	2.693	Covalent
	Se (*4c*)	−0.80			Sn–Se (eq)	0.78	2.863	EDMB
TeO_2	Te (*4a*)	+2.30	Te–O	0.29	Te–O	1.64	1.918	Covalent
	O (*8b*)	−1.15			Te–O	1.06	2.133	EDMB

Species		Löwdin charge	ET		ES		Bond distance (Å)	Bond type
$SbPO_4$	Sb (*2e*)	+2.02	Sb–O_1	0.34	Sb–O_1	1.10	2.024	Covalent
	P (*2e*)	+3.63	Sb–O_2	0.34	Sb–O_2	1.04	2.093	Covalent
	O_1 (*2e*)	−1.39	Sb–O_3	0.34	Sb–O_3	0.80	2.215	EDMB
	O_2 (*2e*)	−1.39	P–O_1	0.36	P–O_1	1.20	1.536	Covalent
	O_3 (*4f*)	−1.44	P–O_2	0.36	P–O_2	1.08	1.555	EDMB
			P–O_3	0.36	P–O_3	1.04	1.566	EDMB
$Sc_2Si_2O_7$	Sc (*4h*)	+1.89	Si–O_1	0.41	Si–O_1	0.68	1.619	EDMB
	Si (*4i*)	+3.16	Si–O_2	0.40	Si–O_2	0.75	1.641	EDMB
	O_1 (*2a*)	−1.63	Si–O_3	0.40	Si–O_3	0.79	1.643	EDMB
	O_2 (*4i*)	−1.40	Sc–O_3	0.63	Sc–O_3	0.89	2.181	Covalent
	O_3 (*8j*)	−1.42	Sc–O_3	0.63	Sc–O_2	0.96	2.102	Covalent
			Sc–O_3	0.63	Sc–O_3	1.18	2.081	Covalent
HF (0 GPa)	H (*4a*)	+0.76	H-F	0.76	H-F	0.98	1.014	Covalent
	F (*4a*)	−0.76			H---F	0.64	1.372	Hydrogen
HF (19 GPa)	H (*4a*)	+0.73	H-F	0.73	H-F	0.86	1.120	ERMB
	F (*4c*)	−0.73						
TlTe	Tl (*16k*)	+0.32	Te_1– Te_2	0.36	Te_1– Te_2	1.40	3.010	ERMB
	Te_1 (*8h*)	−0.41	Te_2– Te_2	0.0	Te_1– Te_2	1.04	3.050	EDMB
	Te_2 (*4b*)	−0.05	Te_3– Te_3	0.0	Te_3– Te_3	1.04	3.050	EDMB
	Te_3 (*4a*)	−0.39						

Table S3. Calculated quantum-chemical bonding descriptors for selected systems discussed in section 4 of the main text using the orbital-based approach as implemented in the LOBSTER software. The Löwdin atomic charges for the different Wyckoff sites, the normalized number of electrons transferred between two atoms (ET), and the number of electrons shared between each atom pair (ES) are provided as well as the bond distances and the bond types. The ES is defined as 2×ICOBI where ICOBI is the Integrated Crystal Orbital Bond Index.

Species	Löwdin charge (Wyck)		ET		ES (2 × ICOBI)		Bond distance (Å)	Bond type
I_3^- (I_1–I_2–I_3)$^-$	I_1	−0.43	I_1–I_2	0.40	I_1-I_2	1.77	2.875	ERMB
	I_2	−0.03	I_2–I_3	0.40	I_2-I_3	1.53	2.954	ERMB
	I_3	−0.43						
XeF_2	Xe	+1.04	Xe–F	0.62	Xe–F	1.76	1.983	ERMB
	F	−0.48						
FHF^-	F	-0.71	F-H	0.43	F-H	0.82	1.159	ERMB
	H	+0.43						
B_2H_6	B	+1.65	B–H_1	0.63	B–H_1	0.68	2.478	EDMB
	H_1	−0.59	B–H_2	0.59	B–H_2	1.21	2.238	Covalent
	H_2	−0.47						
BH_3	B	+1.72	B–H	0.57	B–H	0.95	1.187	Covalent
	H_1	−0.57						
	H_2	−0.57						
	H_3	−0.57						
CsI_3 (I_1–I_2–I_3)$^-$	Cs (*4c*)	+0.65	I_1–I_2	0.36	I_1–I_2	1.08	2.870	ERMB
	I_1 (*4c*)	−0.38	I_2–I_3	0.23	I_2–I_3	0.85	2.990	ERMB
	I_2 (*4c*)	−0.02	Cs–I	0.65	Cs–I	0.15	3.755	Ionic
	I_3 (*4c*)	−0.25						
Cs_2Te_5	Cs_1 (*4c*)	+0.70	Te_1–Te_2	0.33	Te_1–Te_2	0.94	3.060	ERMB
	Cs_2 (*4c*)	+0.64	Te_2–Te_2	0.00	Te_2–Te_2	1.65	2.820	Covalent
	Te_1 (*4c*)	+0.01						
	Te_2 (*16h*)	−0.34						
Cs_2TeI_6	Cs (*8c*)	+0.63	Te–I	0.43	Te–I	0.94	2.925	ERMB
	Te (*4a*)	+0.68	Cs–I	0.63	Cs–I	0.09	4.099	Ionic
	I (*24e*)	−0.32						
TeI_4	Te_1 (*2i*)	+0.63	Te_1–I_1	0.10	Te_1–I_1	1.38	2.799	Covalent
	Te_2 (*2i*)	+0.64	Te_1–I_2	0.15	Te_1–I_2	1.44	2.772	Covalent
	I_1 (*2i*)	−0.10	Te_2–I_8	0.15	Te_2–I_8	1.48	2.760	Covalent

Compound	Site	Charge	Bond	Value	Bond	Value	Distance	Type
	I_2 (*2i*)	−0.15						
	I_3 (*2i*)	−0.19						
	I_4 (*2i*)	−0.22						
	I_5 (*2i*)	−0.26						
	I_6 (*2i*)	−0.15						
	I_7 (*2i*)	−0.15						
	I_8 (*2i*)	−0.15						
Li_2Sb	Li_1 (*3f*)	+0.50	Sb_1–Sb_1	0.0	Sb_1–Sb_1	0.70	3.160	EDMB
	Li_2 (*3g*)	+0.47	Sb_2–Sb_2	0.0	Sb_2–Sb_2	0.70	3.160	EDMB
	Sb_1 (*1b*)	−1.09						
	Sb_2 (*2c*)	−1.00						
$BaZnSb_2$	Ba (*4e*)	+1.17	Sb_1–Sb_1	0.0	Sb_1–Sb_1	0.80	3.242	EDMB
	Zn (*4d*)	+1.03	Zn–Sb_2	0.52	Zn–Sb_2	0.89	2.770	Covalent
	Sb_1 (*4c*)	−0.82	Ba–Sb_2	0.62	Ba–Sb_2	0.11	3.486	Ionic
	Sb_2 (*4e*)	−1.86						
α-GeTe	Ge (*3a*)	+0.18	Ge–Te	0.09	Ge–Te	1.11	2.848	EDMB
	Te (*3a*)	−0.18						
SnSe	Sn (*4c*)	+0.20	Sn–Se	0.1	Sn–Se(ax)	1.20	2.693	Covalent
	Se (*4c*)	−0.20			Sn–Se(eq)	0.72	2.863	EDMB
TeO_2	Te (*4a*)	+1.86	Te–O	0.23	Te–O	1.50	1.918	Covalent
	O (*8b*)	−0.93			Te–O	0.90	2.133	EDMB
$SbPO_4$	Sb (*2e*)	+2.13	Sb–O_1	0.36	Sb–O_1	1.18	2.024	Covalent
	P (*2e*)	+1.46	Sb–O_2	0.36	Sb–O_2	1.04	2.093	Covalent
	O_1 (*2e*)	−0.87	Sb–O_3	0.36	Sb–O_3	0.74	2.215	EDMB
	O_2 (*2e*)	−0.89	P–O_1	0.15	P–O_1	1.84	1.536	Covalent
	O_3 (*4f*)	−0.91	P–O_2	0.15	P–O_2	1.76	1.555	Covalent
			P–O_3	0.15	P–O_3	1.68	1.566	Covalent
$Sc_2Si_2O_7$	Sc (*4h*)	+2.48	Si–O_1	0.26	Si–O_1	1.04	1.619	EDMB
	Si (*4i*)	+0.93	Si–O_2	0.12	Si–O_2	1.24	1.641	Covalent
	O_1 (*2a*)	−1.05	Si–O_3	0.12	Si–O_3	1.26	1.643	Covalent
	O_2 (*4i*)	−1.00	Sc–O_3	0.83	Sc–O_3	0.55	2.181	Ionic
	O_3 (*8j*)	−0.99	Sc–O_3	0.83	Sc–O_2	0.64	2.102	Ionic
			Sc–O_3	0.83	Sc–O_3	0.72	2.081	Ionic
HF (0 GPa)	H (*4a*)	+0.44	H-F	0.44	H–F	1.08	1.014	Covalent
	F (*4a*)	−0.44			H---F	0.48	1.372	Hydrogen
HF (19 GPa)	H (*4a*)	+0.41	H-F	0.41	H-F	0.80	1.120	ERMB
	F (*4c*)	−0.41						
TlTe	Tl (*16k*)	+0.09	Te_1–Te_2	0.08	Te_1–Te_2	0.88	3.010	ERMB
	Te_1 (*8h*)	−0.14	Te_2–Te_2	0.0	Te_1–Te_2	0.65	3.050	EDMB
	Te_2 (*4b*)	−0.06	Te_3–Te_3	0.0	Te_3–Te_3	0.65	3.050	EDMB
	Te_3 (*4a*)	−0.11						

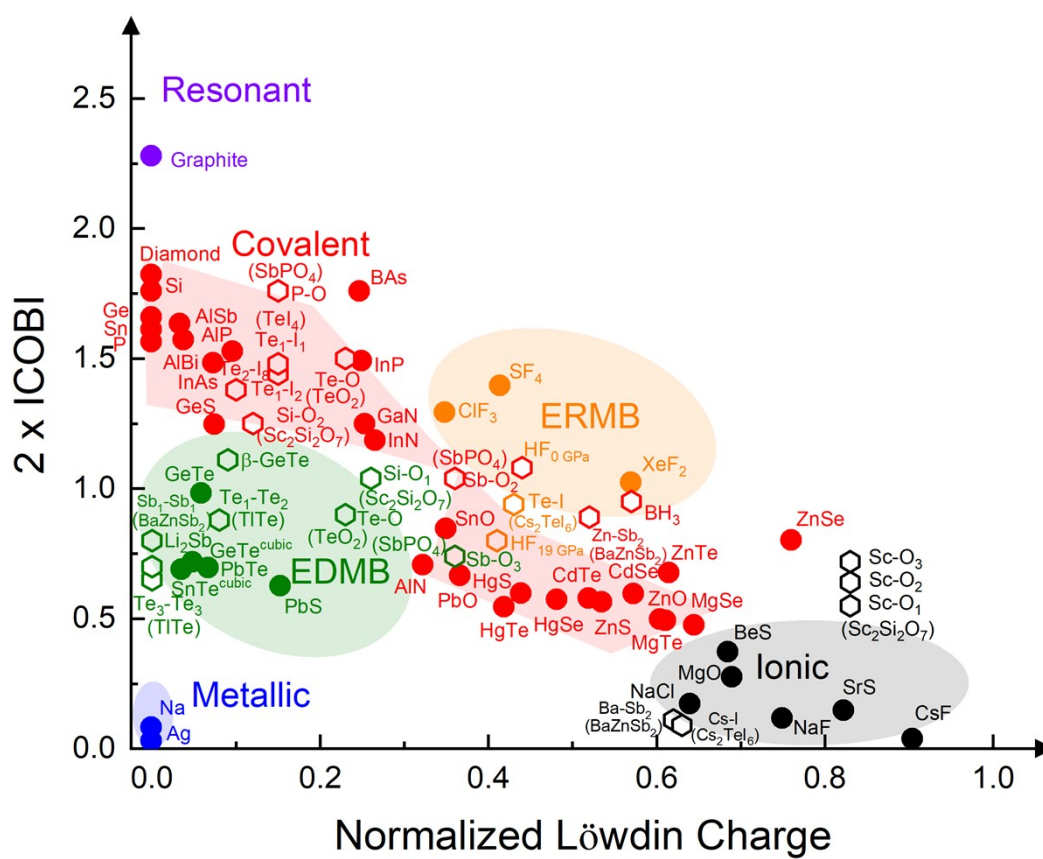## 2.2. Orbital-based ES vs. ET map.

Figure S1. 2D map of the number of electrons shared (ES) vs. the normalized number of electrons transferred (ET) showing the chemical bond classification in materials using the orbital-based approach as implemented in LOBSTER program. The ES is considered as twice the bond order obtained from the integrated crystal orbital bond index for two centers (ICOBI(2c), here simply specified as ICOBI). On the other hand, the ET is obtained by renormalizing the Löwdin charge calculated using the formal oxidation state (orbital-based calculation).

2.3. Three-stage process of multicenter bond formation in several trimers.

The concepts of the core, valence, and van der Waals spheres of Echeverría and Álvarez,[33,34] allow us to see the three stages of the mechanism of ERMB formation in the I_3^- anion from the original I_2 and I^- entities, as described in **Fig. S2**. Note that the valence sphere of the I atom is defined as the sphere whose radius is the single covalent bond length between two I atoms in the I_2 molecule.
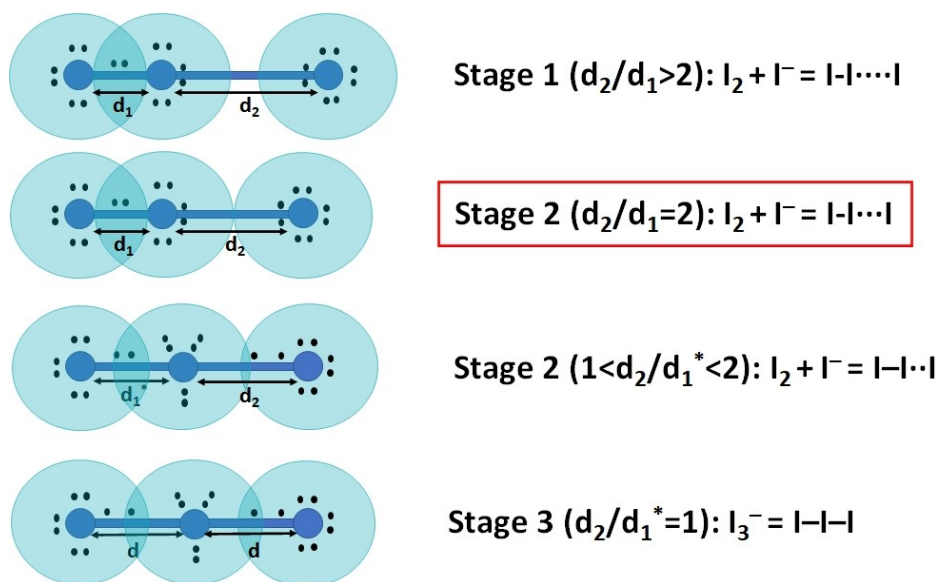
Figure S2. Schematic picture of the three stages of formation of the electron-rich multicenter bond in the I_3^- polyanion (from the original I_2 molecule and I^- ion) using the concept of valence spheres of the different atoms. The start of stage 2 is the step going from a supramolecular non-covalent closed shell interaction of electrostatic origin to a secondary non-covalent interaction with a mixture of closed shell and share shell interactions which marks the onset of quantum interactions.

In stage 1, both I_2 and I^- entities are separated at a distance d_2 which is more than twice the distance d_1 of the single covalent bond in the I_2 molecule, i.e., more than twice the valence sphere radius. Consequently, the valence sphere of the I^- ion does not interact with the valence sphere of the atoms in the I_2 molecule and the interaction between both entities is a supramolecular non-covalent interaction of electrostatic nature. In other words, while the primary single covalent bond inside the I_2 molecule is a shared shell interaction, the secondary interaction, if it exists, between I_2 and I^- is a closed shell interaction.[33,34]

When $d_2 = 2d_1$, both I_2 and I^- entities are separated at a distance d_2 which is exactly twice the distance d_1 of the single covalent bond in the I_2 molecule. In this context, the valence sphere of the I^- ion starts interacting with the valence sphere of the atoms in the I_2 molecule. This is the starting point of stage 2 and the start of the quantum interactions that lead to the redistribution of charge and the formation of molecular orbitals suggested by Espinosa et al.[35]

When $d_2 < 2d_1$, there is an overlap of the valence spheres of the I_2 molecule and the I^- ion so that there is a *trans influence* of the secondary bond in the primary bond that causes an enlargement of d_1 (noted as d_1^* in **Fig. S2**). As a consequence of the *trans influence* and to satisfy the octet rule, there is a charge redistribution or charge shift of the electrons inside the covalent bond of I_2 towards the external atom of the asymmetric I_3^- polyanion. The enlargement of the primary bond

and the charge shift towards the external or terminal atom proceeds until both d_1^* and d_2 distances become equal or almost equal. When this happens, the multicenter bond is formed as corresponds to stage 3. Due to the shift of electrons towards the external atoms, only 8 electrons occupy the valence sphere of the central atom of the I_3^- polyanion, so that the octet rule is satisfied for all the three atoms of the I_3^- polyanion as observed in the bottom of **Fig. S2**. Moreover, the extra electrons are allocated at the van der Waals sphere (red sphere) as plotted in **Fig. 5** (see main text).

Another clear example of the three-stage process in the ERMB formation with the start of stage 2 of multicenter interaction occurring when $d_2/d_1 = 2$ is provided by FHF$^-$ molecule. Espinosa *et al.* showed that stage 2 in the formation of the formation of the above molecule takes place when the H$\cdots$F secondary bonding reaches a value around 1.9 Å.[33,34] This value is ca. the double of the covalent H—F bond (ca. 0.92 Å).[36]

Finally, a clear example of the three-stage process in the EDMB formation with the start of stage 2 of multicenter interaction occurring when $d_2/d_1 = 2$ is provided by hydrogen under compression. V. Labet *et al.* simulated the evolution of the shortest and second shortest H—H distances in the different phases of dense H_2.[37–40] They found that the shortest interatomic distance, corresponding to the primary covalent bond in H_2 (d_1 in our theory), decreases in a normal way with compression up to 100 GPa and shows an anomalous increase above this pressure up to 500 GPa, while the second shortest H—H distance –which could be attributed to a secondary non-covalent bond (d_2 in our theory)–, decreases all the way up to 500 GPa. The change in the behavior of the primary bond that occurs around 100 GPa takes place exactly when the secondary bond distance (ca. 1.46 Å) is twice the primary bond distance (ca. 0.73 Å) as can be observed in Figures 6 and 7 in Ref. [37]. As a consequence of the multicenter interaction occurring in dense H_2 between 100 GPa and 500 GPa, this system is expected to lead to the formation of EDMBs above 500 GPa in which each H would be equally bonded to other two H atoms and where there would be a single electron shared every two H atoms, as recently demonstrated.[40]

The unique and paradigmatic example of dense H_2 thus provides clear proof of the three stages of formation of multicenter bonds proposed in this paper and the start of the multicenter interaction (stage 2) when $d_2/d_1=2$. Therefore, it seems clear that the formation of multicenter bonds (ERMBs and EDMBs), at least in molecules as we have discussed here, has three stages in which stage 2 starts when $d_2/d_1=2$. In solids, such as in solid arsenic, the pressure-induced formation of EDMBs has been shown to start in stage 2 at a much smaller d_2/d_1 ratio.[41,42] At present, we cannot provide an explanation for the different behavior in molecules and solids regarding the different ratio for the start of stage 2 in multicenter bond formation, but this different behavior is likely correlated with the different bond lengths of covalent bonds in molecules and solids; e.g. the I—I covalent bond in the I_2 molecule has a bond length of 2.66 Å in the gas phase[43] and of 2.70 Å in the solid phase.[44] Therefore, the larger bond lengths of covalent d_1 bonds in solids is consistent with a smaller d_2/d_1 ratio for the start of stage 2 in solids than in free molecules.

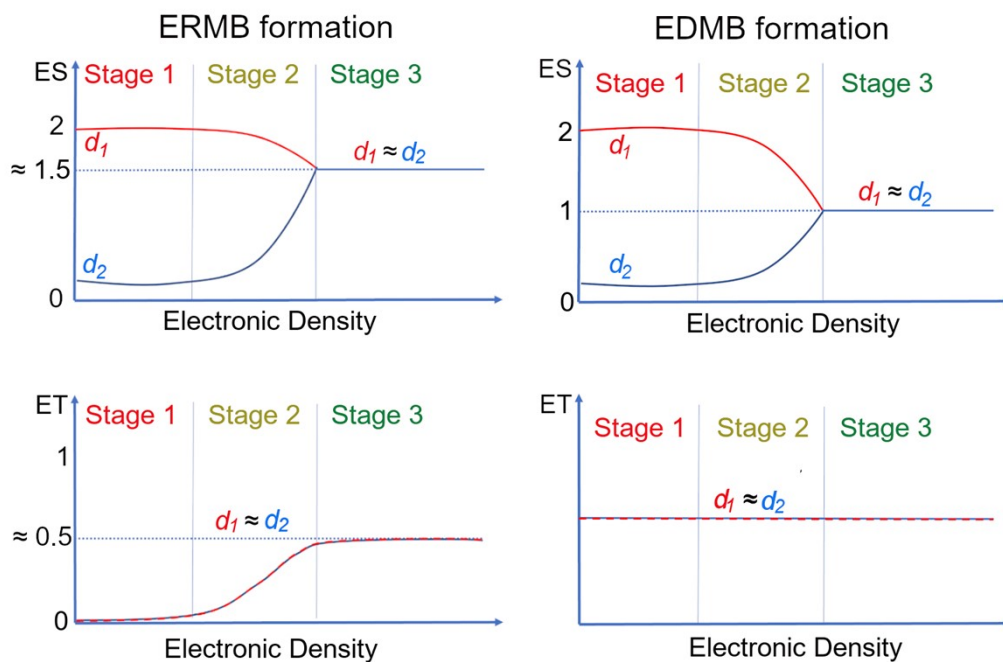## 2.4. Behaviour of ES and ET values in multicenter bond formation.

Figure S3. Schematic evolution of the ES and ET values in the formation of ERMBs (left) and EDMBs (right).
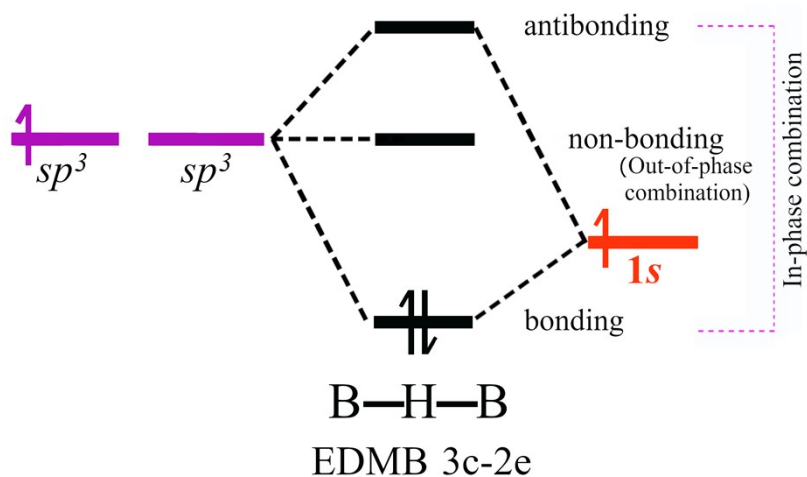
2.5. Molecular orbitals in B_2H_6.

Figure S4. Schematic molecular orbital (MO) diagram for 3c-2e electron-deficient multicenter bond (EDMB) formation in the B_2H_6 molecule.
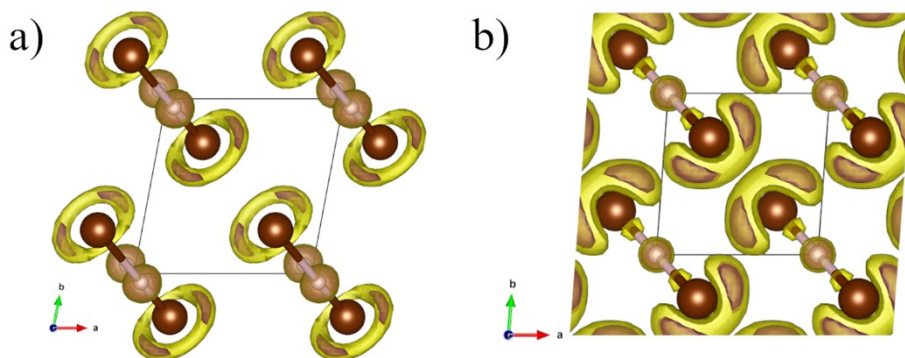
2.6. HF under compression.

Figure S5. 3D isosurfaces of ELF in HF at a) 0 GPa (isosurface value in the range 0.82 - 0.85) and b) 19 GPa (isosurface value in the range of 0.81 - 0.84). White and brown balls represent H and F atoms, respectively. The transformation of ELF isosurfaces from a toroidal shape at 0 GPa to a cashew-like shape at 19 GPa is consistent with the loss of one LEP by F atoms, so that the two electrons of the loosed LEP become bonding electrons at the H–F bonds at both sides of F atoms.

The distorted spherical ELF attractor of H atoms along the H–F bond path contains 1.72e. The charge localized along the H–F bond forms one isosurface with the 1s electron of H. They can NOT be separated. Two separate attractors (brown) around F atoms are obtained at an isosurface value of 0.85 which changes to a ring (yellow) at 0.82 containing 6.53e as shown in **Fig. S5a**. The three LEPs don't contribute to the bonding in this case. The ELF increases smoothly along the bonding path H–F.

At higher pressure, 19 GPa, the H spherical isosurface has a smaller volume than that at room pressure containing only 0.75e. Herein, there is a maximum of ELF at the H–F bond critical point of a value of 0.71e. An ELF isosurface with a value of 0.84 shows two attractors (brown) around F atoms which converts to a cashew-like isosurface when it decreases to 0.84 having in total 5.8 e as depicted in **Fig. S5b**.

One ELF attractor appears in the shape of a cone (distorted sphere) that includes the one electron of H and the other part that comes from the F atom (1.6 e). The two charges can NOT be separated whatever the value of the ELF isosurface. It always appears as if it is one charge accumulation along the bonding path.
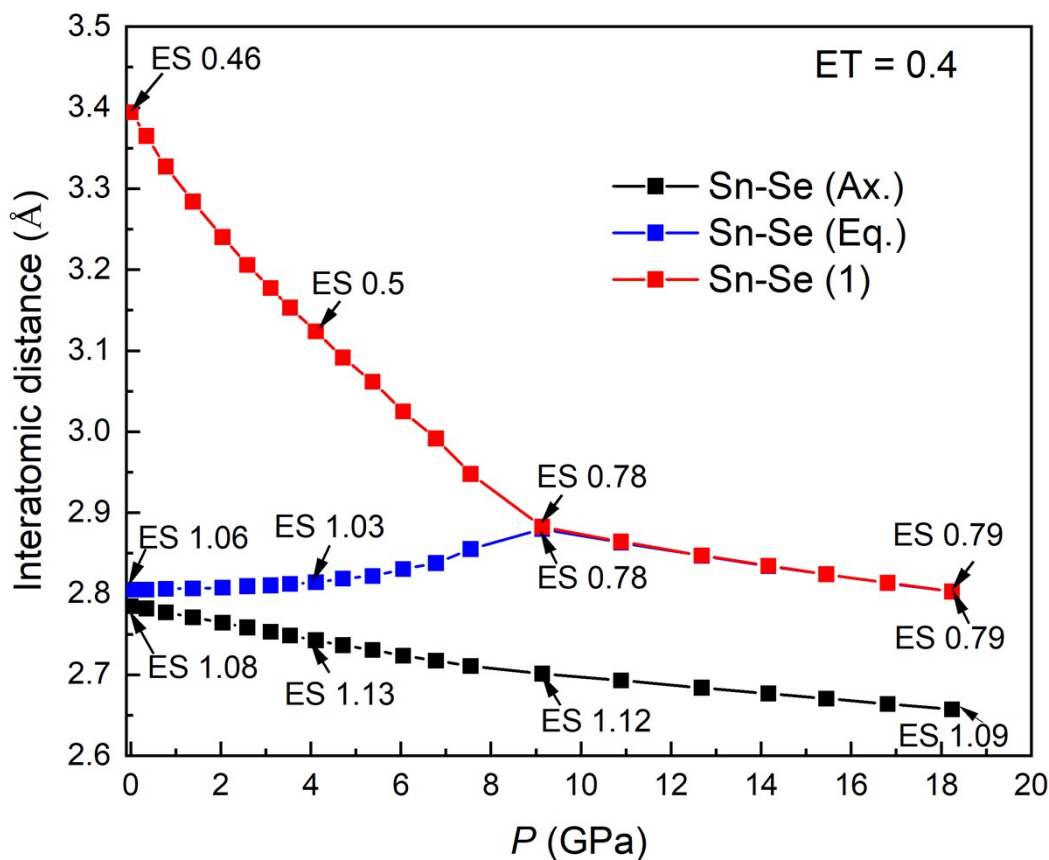
2.7. SnSe under compression.

Figure S6. Pressure dependence of the bond lengths of primary (covalent) and secondary (noncovalent) bonds in SnSe. ES values obtained with CRITIC2 at different pressures are indicated. The ET value is roughly constant (around 0.4) in the whole pressure range calculated. Black symbols correspond to the covalent axial bond in both the *Pnma* (below 10 GPa) and *Cmcm* (above 10 GPa) phases. Blue symbols correspond to covalent equatorial bonds in the *Pnma* phase that form EDMBs in the *Cmcm* phase (see **Fig. 1**).

The iono-covalent (EDMB) nature of the axial (equatorial) bonds at the *Cmcm* phase of SnSe are confirmed by our ES and ET values (see **Table S2 and Fig. S6**). In the *Cmcm* phase of SnSe and GeSe, the quasi-linear 2D EDMBs can be observed perpendicular to the *b*-axis (see **Fig. 8b**). More specifically, in the *Cmcm* phase of SnSe, both Sn and Se atoms are located in *4c* sites and there are two types of Sn—Se bonds at 10 GPa. There is a short Sn—Se bond ($d \approx 2.70$ Å) perpendicular to the layers and four long Se—Se bonds ($d \approx 2.85$ Å) quasi-parallel to the layers at 10 GPa.[45–47] The Sn and Se atoms have Bader [Löwdin] charges of 0.80 [0.20] and the calculated short (long) Sn—Se bond has a bond distance of 2.69 Å (2.86 Å) at 10 GPa (see **Table S2 and Fig. S6**). The short (long) Sn—Se bond has an ES value of 1.10 [1.20] (0.78 [0.72]) while the ET value of both bonds is around 0.4 [0.1] obtained from the Bader [Löwdin] charge of the Sn atom. Therefore, the short (long) Sn—Se bond can be classified as iono-covalent (EDMB) according to the location in **Fig. 1** and **Fig. S1**.

The clear distinction between the iono-covalent bonds and EDMBs in the *Cmcm* phase of TlI at RP is not so easy as in the *Cmcm* phase of SnSe at HP. At RP, the Tl atom has a Bader [Löwdin] charge of 0.46 [0.07] and there is an experimental short Tl—I bond (d = 3.346 Å) perpendicular to the layers and four long Tl—I bonds (d= 3.491 Å) quasi-parallel to the layers,[48] while the calculated short (long) Tl—I bond has a bond distance of 3.288 Å (3.448 Å) (see **Tables S2 and S3**). The short (long) Tl—I bond has an ES value of 1.8 [0.74] (1.1 [0.5]) while the ET value of both bonds is 0.46 [0.07] obtained as the Bader [Löwdin] charge of the Tl atom. Therefore, both short and long Tl—I bonds can be classified as EDMBs according to the location in **Fig. 1** and **Fig. S1**. This situation, also found for InBr and InI at RP (not here shown), is different to that described for the *Cmcm* phase of SnSe in the previous paragraph. We consider that the reason for the EDMB character of the Tl—I bond perpendicular to the layer plane in the *Cmcm* phase is that this bond has already lost charge due to the interaction with two neighbor atoms in the adjacent layer so that the coordination of atoms in TlI at RP (also in InBr and InI at RP) cannot be considered to be five but five + two. Therefore, part of the charge of the iono-covalent Tl—I bond perpendicular to the layer plane is now shared with two atoms of the adjacent layer which causes its partial EDMB character.
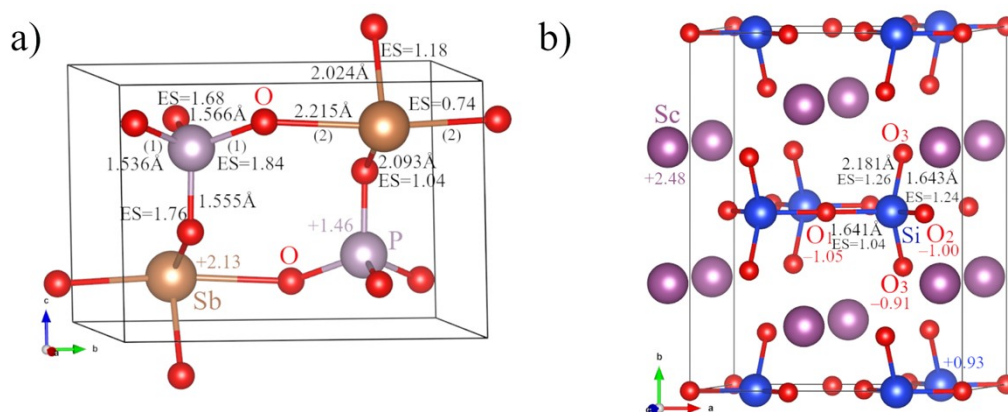
2.8. Examples of $SbPO_4$ and $Sc_2Si_2O_7$.

Figure S7. Details of the crystal structures of (a) $SbPO_4$ and (b) $Sc_2Si_2O_7$. These solids show heteropolar 1D EDMBs. Details on bond distances, Löwdin atomic charges, ET, and ES of various bonds are illustrated here and summarized in **Table S3**.

$SbPO_4$. One example of quasi-linear 1D EDMB is that formed by Sb and O bonds in $SbPO_4$ (see **Fig. S7a**).[29] In $SbPO_4$, P is four-fold coordinated with two short bonds (d = 1.536 Å) and two slightly longer bonds (d = 1.555 and 1.566 Å) to O atoms in a sp^3 geometry (if we consider that the O atoms have two LEPs not plotted in **Fig. S7a**). However, Sb is fourfold coordinated to O atoms, with two short (d = 2.024 and 2.093 Å) and two long Sb–O bonds (d = 2.215 Å), forming a see-saw geometry (if we consider that Sb^{3+} has a single LEP not plotted in **Fig. S7a**). The two

short (long) Sb–O bonds have ES= 1.10 [1.18] (0.8 [0.74]) and both have ET= 0.34 [0.36] according to CRITIC2 [LOBSTER] software. Note that the ET value is calculated by dividing the Bader [Löwdin] charge of Sb (+2.02 [+2.13]) by the absolute nominal valence of Sb in this compound (+3). In addition, this value must be divided by the multiplicity ratio between the Sb and all O Wyckoff sites (2), which in turn, is the average number of O atoms to which the charge of Sb is transferred. Note that this is similar to assuming that $SbPO_4$ is like a SbO_2 + PO_2 compound, so we proceed as in TeO_2 (see main text). This means that the short (long) bonds are located in the red (orange) regions of covalent bonds (EDMBs) in **Fig. 1** in the main text. Note that the same reasoning can be done for the P–O bonds with ES values between 1.04 [1.68] and 1.2 [1.84] and ET value of 0.36 [0.15]. This ET value is obtained by dividing the Bader [Löwdin] charge of P (+3.63 [+1.46]) by the nominal valence of P (+5) and by the difference in multiplicity between P and O atoms (2), which is the average number of O atoms to which the charge of P is transferred. It can be observed that with these numbers the P–O bonds can be classified as two short covalent bonds (ES = 1.2) and two slightly longer EDMBs (ES = 1.04–1.08) according to QTAIM, while they are all covalent P–O bonds (ES ≈ 1.68–1.84) according to LOBSTER. We consider that the picture provided by LOBSTER values for $SbPO_4$ is more accurate than that provided by QTAIM values since all experimental P–O bond lengths are very similar (within 0.05 Å). All in all, the short (long) Sb–O bonds are located in the red (orange) regions of covalent bonds (EDMBs) as shown in **Fig. 1** and **Fig. S1**.

$Sc_2Si_2O_7$. Another example of linear 1D EDMB is the Si–O–Si bonds within the $[O_3Si–O–SiO3]^{6-}$ polyanion in solid $Sc_2Si_2O_7$ silicate (**Fig. S7b**). The Bader [Löwdin] charges of the different atoms are: $Sc^{1.89+[2.48+]}$, $Si^{3.15+[0.93+]}$, and $O^{1.48-[1.00-]}$. The terminal (central) Si–O bond has a calculated bond distance of 1.641 Å (1.619 Å) that agrees with the experimental value 1.632 Å (1.606 Å). The terminal (central) Si–O bond has an ES value of 0.74 [1.25] (0.68 [1.04]). On the other hand, this compound is the most complex to obtain the ET values since two cations give charge to three anions, in addition, the three anions have different multiplicities. Moreover, Sc atoms are only bonded to O2 and O3 atoms, while Si atoms are bonded to O1, O2, and O3 atoms. This means that Sc atoms can be considered to give charge to O2 and O3 atoms, while Si atoms give charge to O1, O2, and O3 atoms. To obtain the ET values we can proceed as follows. First, the ET value of the Si–O1 bond can be obtained by dividing the Bader [Löwdin] charge by the nominal valence of O (2). In addition, this value must be divided by 2 because the charge of O1 (located between the two Si atoms) is provided by the two Si atoms (this yields ET = 0.41 [0.26]). Second, the ET value of the Si–O2 and Si–O3 bonds can be calculated by obtaining the Bader [Löwdin] charge of Si that it gives to the O2 and O3 atoms. This charge is the total Bader [Löwdin] charge of Si (3.15 [0.93]) minus the charge given to the O1 atom (1.05/2). This value must be divided by the nominal valence of Si (4) and the multiplicity factor between Si and O2 and O3 (1.5) because the charge

of Si is given one O2 and two O3 atoms (this yields ET = 0.40 [0.12]). On other hand, the ET values of the Sc-O_2 and Sc-O_3 bonds can be obtained by dividing the Bader [Löwdin] charge of Sc by the nominal valence of Sc (3). As observed, there is a discrepancy not only in the Bader and Löwdin charges but also in the ES and ET values between density-based and orbital-based methods. While density-based methods suggest that all Si–O bonds are EDMBs and all Sc–O bonds are covalent, orbital-based methods suggest that Sc–O, terminal Si–O bonds, and central Si–O bonds are ionic, covalent, and EDMBs, respectively. Therefore, the terminal (central) heteropolar Si–O bonds can be classified as covalent bonds (EDMBs) according to **Fig. S1**. The Löwdin charges and the ES and ET values obtained from LOBSTER fully agree with the hypothesis of Vegas and coworkers,[49,50] who considered that the two Sc atoms would give all their charge to the Si_2O_7 entity to form $[O_3Si–O–SiO_3]^{6-}$ polyanion which form linear Si–O_1–Si 3c-2e bonds. Curiously, this point of view is not supported by density-based methods that shows an anomalous small Bader charge for Sc atoms and an anomalous large Bader charge for Si atoms, as if Si atoms would give more charge than Sc atoms, contrary to common understanding.

It must be noted $Sc_2Si_2O_7$ constitutes an extraordinary case of 1D EDMB compared to the aforementioned examples since the Si—O bond distance in the EDMB is shorter than that of the Si—O bond distance in the covalent bond (as if the EDMB was "compressed"). At the moment, we do not have an explanation for this extraordinary finding since usually EDMBs are longer than covalent bonds at the same pressure and temperature conditions. However, it is curious that electron-deficient Si—O bonds; i.e. with rather small ES values have been already found within zeolite rings, such as the 4MR (simulated as a $Si_4O_4H_8$ molecule), in faujasite.[51] Calculations with QTAIM have shown a delocalization index (DI) of 0.39, corresponding to an ES (2 x DI) value of 0.78; a value that is of the same order as the one found by us (0.68) using QTAIM in the linear Si—O_1—Si EDMB in $Sc_2Si_2O_7$. In addition, we have found that the ET value of the Si—O bond in faujasite is 0.42 (Bader charge of O (–1.65) divided by 4 because it must be divided by the nominal valence of O (2) and by an additional 2, which is the factor of different multiplicity between the donor, Si, and the acceptor, O, in the *Fd-3m* structure of faujasite). The relatively small ET value (0.42) is similar to the ET value of 0.41 we have found for the linear Si—O_1 bond in $Sc_2Si_2O_7$. We acknowledge the conflict between the two methods observed in this case and others. We plan to study this phenomenon in greater detail in future work to better understand its origin and implications.

2.9. Examples of SbOF and TiPO$_4$-V.

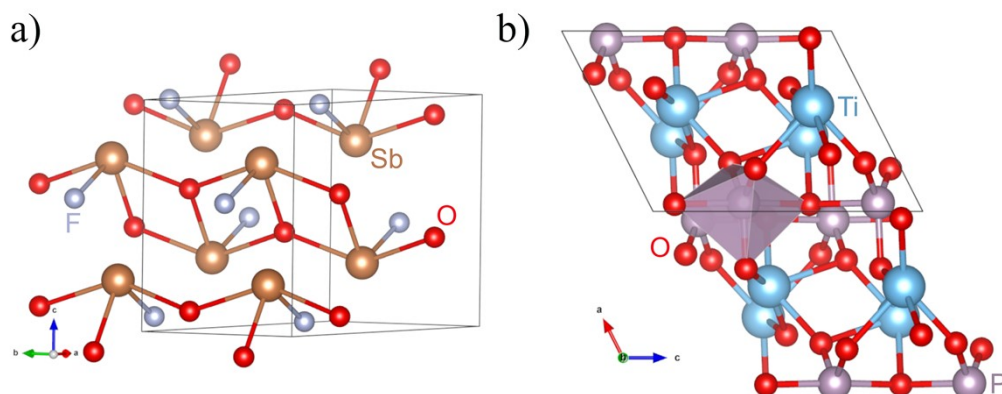**Figure S8.** Crystal structures of (a) SbOF and (b) TiPO$_4$-V. SbOF shows the A(1,2,1) unit for the O atom and the A(2,1,1) unit for the Sb atom. The TiPO$_4$-V phase shows the A(3,0,1) unit for the P atom.

References

1   G. Kresse and J. Furthmüller, *Phys. Rev. B*, 1996, **54**, 11169–11186.

2   G. Kresse and J. Furthmüller, *Comput. Mater. Sci.*, 1996, **6**, 15–50.

3   G. Kresse and D. Joubert, *Phys. Rev. B*, 1999, **59**, 1758–1775.

4   J. P. Perdew, K. Burke and M. Ernzerhof, *Phys. Rev. Lett.*, 1996, **77**, 3865–3868.

5   P. E. Blöchl, *Phys. Rev. B*, 1994, **50**, 17953–17979.

6   J. P. Perdew, A. Ruzsinszky, G. I. Csonka, O. A. Vydrov, G. E. Scuseria, L. A. Constantin, X. Zhou and K. Burke, *Phys. Rev. Lett.*, 2008, **100**, 136406.

7   H. J. Monkhorst and J. D. Pack, *Phys. Rev. B*, 1976, **13**, 5188–5192.

8   P. Giannozzi, O. Andreussi, T. Brumme, O. Bunau, M. Buongiorno Nardelli, M. Calandra, R. Car, C. Cavazzoni, D. Ceresoli, M. Cococcioni, N. Colonna, I. Carnimeo, A. Dal Corso, S. de Gironcoli, P. Delugas, R. A. DiStasio, A. Ferretti, A. Floris, G. Fratesi, G. Fugallo, R. Gebauer, U. Gerstmann, F. Giustino, T. Gorni, J. Jia, M. Kawamura, H.-Y. Ko, A. Kokalj, E. Küçükbenli, M. Lazzeri, M. Marsili, N. Marzari, F. Mauri, N. L. Nguyen, H.-V. Nguyen, A. Otero-de-la-Roza, L. Paulatto, S. Poncé, D. Rocca, R. Sabatini, B. Santra, M. Schlipf, A. P. Seitsonen, A. Smogunov, I. Timrov, T. Thonhauser, P. Umari, N. Vast, X. Wu and S. Baroni, *J. Phys.: Condens. Matter*, 2017, **29**, 465901.

9   A. A. Mostofi, J. R. Yates, Y.-S. Lee, I. Souza, D. Vanderbilt and N. Marzari, *Comput. Phys. Commun.*, 2008, **178**, 685–699.

10   A. Otero-de-la-Roza, E. R. Johnson and V. Luaña, *Comput. Phys. Commun. *, 2014, **185**, 1007–1018.

11   A. Dal Corso, *Comput. Mater. Sci.*, 2014, **95**, 337–350.

12   A. Otero-de-la-Roza, Á. Martín Pendás and E. R. Johnson, *J. Chem. Theory Comput.*, 2018, **14**, 4699–4710.

13   S. Maintz, V. L. Deringer, A. L. Tchougréeff and R. Dronskowski, *J. Comput. Chem.*, 2016, **37**, 1030–1035.

14   S. Maintz, V. L. Deringer, A. L. Tchougréeff and R. Dronskowski, *J. Comput. Chem.*, 2013, **34**, 2557–2567.

15   R. Nelson, C. Ertural, J. George, V. L. Deringer, G. Hautier and R. Dronskowski, *J. Comput. Chem.*, 2020, **41**, 1931–1940.

16   P. C. Müller, C. Ertural, J. Hempelmann and R. Dronskowski, *J. Phys. Chem. C*, 2021, **125**, 7959–7970.

17   K. L. Schuchardt, B. T. Didier, T. Elsethagen, L. Sun, V. Gurumoorthi, J. Chase, J. Li and T. L. Windus, *J. Chem. Inf. Model.*, 2007, **47**, 1045–1052.

18   B. P. Pritchard, D. Altarawy, B. Didier, T. D. Gibson and T. L. Windus, *J. Chem. Inf. Model.*, 2019, **59**, 4814–4820.

19   A. K. Todd, *TK Gristmill Software, Overland Park KS, USA. (Aim.Tkgristmill.Com)*.

20   T. Poręba, S. Racioppi, G. Garbarino, W. Morgenroth and M. Mezouar, *Inorg. Chem.*, 2022, **61**, 10977–10985.

21   P. Boettcher and U. Kretschmann, *Z. anorg. allg. chem.*, 1982, **491**, 39–46.

22   L. M. Manojlovic, *Bull. Inst. Nuclear Sci. 'Boris Kidrich'*, 1956, **6**, 149–152.

23   P. Schneiderhan, P. Schmidt, M. Ströbele, C. P. Romao and H.-J. Meyer, *Cryst. Growth Des.*, 2020, **20**, 3780–3784.

24   R. Gérardin and J. Aubry, *J. Comptes Rendus des Seances de l'Academie des Sciences, Serie C: Sciences Chimiques*, 1974, **278**, 1097–1098.

25   E. Brechtel, G. Cordier and H. Schäfer, *J. Less-Common Met.*, 1981, **79**, 131–138.

26   M. Samanta, T. Ghosh, R. Arora, U. V. Waghmare and K. Biswas, *J. Am. Chem. Soc.*, 2019, **141**, 19505–19512.

27   R. Vasudevan, L. Zhang, Q. Ren, J. Wu, Z. Cheng, J. Wang, S. Lin, F. Zhu, Y. Zhang, M. Hölzel, Y. Pei, X. Tong and J. Ma, *J. Alloys Compd.*, 2022, **923**, 166251.

28   T. G. Worlton and R. A. Beyerlein, *Phys. Rev. B*, 1975, **12**, 1899–1907.

29   A. L. de J. Pereira, D. Santamaría-Pérez, R. Vilaplana, D. Errandonea, C. Popescu, E. L. da Silva, J. A. Sans, J. Rodríguez-Carvajal, A. Muñoz, P. Rodríguez-Hernández, A. Mujica, S. E. Radescu, A. Beltrán, A. Otero-de-la-Roza, M. Nalin, M. Mollar and F. J. Manjón, *Inorg. Chem.*, 2020, **59**, 287–307.

30   E. E. Foord, S. D. Birmingham, F. Demartin, T. Pilati, C. M. Gramaccioli and F. E. Lichte, *Canad. Mineral*, 1993, **31**, 337–346.

31   M. W. Johnson, E. Sándor and E. Arzi, *Acta Cryst.*, 1975, **31**, 1998–2003.

32   K. Stöwe, *J. Solid State Chem.*, 2000, **149**, 123–132.

33   J. Echeverría and S. Alvarez, *Chem. Sci.*, 2023, **14**, 11647–11688.

34   J. Echeverría and S. Alvarez, *Chem. Sci.*, 2024, **15**, 12166–12168.

35   E. Espinosa, I. Alkorta, J. Elguero and E. Molins, *J. Chem. Phys.*, 2002, **117**, 5529–5542.

36   G. H. F. Diercksen, W. von Niessen and W. P. Kraemer, *Theo. chim. acta*, 1973, **31**, 205–214.

37   V. Labet, P. Gonzalez-Morelos, R. Hoffmann and N. W. Ashcroft, *J. Chem. Phys.*, 2012, **136**, 074501.

38   V. Labet, R. Hoffmann and N. W. Ashcroft, *J. Chem. Phys.*, 2012, **136**, 074502.

39   V. Labet, R. Hoffmann and N. W. Ashcroft, *J. Chem. Phys.*, 2012, **136**, 074503.

40   V. Riffet, V. Labet and J. Contreras-García, *Phys. Chem. Chem. Phys.*, 2017, **19**, 26381–26395.

41   H. H. Osman, A. Otero-de-la-Roza, P. Rodríguez-Hernández, A. Muñoz and F. J. Manjón, *10.26434/chemrxiv-2023-pv66p-v2*.

42   H. H. Osman, A. Otero-de-la-Roza, P. Rodríguez-Hernández, A. Muñoz and F. J. Manjón, *J. Mater. Chem. C*, 2024, **12**, 10447–10474.

43   R. S. Mulliken, *J Chem Phys*, 1971, **55**, 288–309.

44   P. M. Harris, E. Jr. Mack and F. C. Blake, *J Am Chem Soc*, 1928, **50**, 1583–1600.

45   I. Loa, R. J. Husband, R. A. Downie, S. R. Popuri and J.-W. G. Bos, *J. Phys: Condens. Matter*, 2015, **27**, 072202.

46   M. Xu, S. Jakobs, R. Mazzarello, J.-Y. Cho, Z. Yang, H. Hollermann, D. Shang, X. Miao, Z. Yu, L. Wang and M. Wuttig, *J. Phys. Chem. C*, 2017, **121**, 25447–25454.

47   I. Efthimiopoulos, M. Berg, A. Bande, L. Puskar, E. Ritter, W. Xu, A. Marcelli, M. Ortolani, M. Harms, J. Müller, S. Speziale, M. Koch-Müller, Y. Liu, L.-D. Zhao and U. Schade, *Phys. Chem. Chem. Phys.*, 2019, **21**, 8663–8678.

48   L. Helmholz, *Z. Kristallogr. Cryst. Mater.*, 1936, **95**, 129–137.

49   Á. Vegas, R. Notario, E. Chamorro, P. Pérez and J. F. Liebman, *Acta Cryst.*, 2013, **69**, 163–175.

50   Á. Vegas, *Structural Models of Inorganic Crystals*, Universitat Politècnica de València, 1st ed., 2018.

51   C. Gatti, G. Ottonello and P. Richet, *J. Phys. Chem. A*, 2012, **116**, 8584–8598.